# Chemical Analysis for Alkali Ion–exchanged Glass Using Atom Probe Tomography

Se-Ho Kim, Leigh T Stephenson, Torsten Schwarz, Baptiste Gault

*Microscopy and Microanalysis*, 2023, **00**, 1–10
https://doi.org/10.1093/micmic/ozad034

**Original Article**

Microscopy AND Microanalysis

# Chemical Analysis for Alkali Ion–exchanged Glass Using Atom Probe Tomography

**Se-Ho Kim[1,2,*], Leigh T. Stephenson[1], Torsten Schwarz[1], and Baptiste Gault[1,3,*]**

[1]*Microstructure Physics and Alloy Design, Max-Planck-Institut für Eisenforschung, Max-Planck-Straße 1, 40237 Düsseldorf, Germany*
[2]*Department of Materials Science and Engineering, Korea University, 145 Anam-ro, Seongbuk-gu, Seoul 02841, South Korea*
[3]*Department of Materials, Imperial College London, Royal School of Mines, Prince Consort Rd, South Kensington, London SW7 2AZ, UK*

***Corresponding authors:** Se-Ho Kim, E-mail: sehonetkr@korea.ac.kr; Baptiste Gault, E-mail: b.gault@mpie.de

## Abstract

The developing flexible ultrathin glass for use in foldable displays has attracted widespread attention as an alternative to rigid electronic smartphones. However, the detailed compositional effects of chemically strengthened glass are not well understood. Moreover, the spatially resolved chemistry and depth of the compression layer of tempered glass are far from clear. In this study, commonly used X-ray spectroscopy techniques and atom probe tomography (APT) were used comparatively to investigate the distribution of constituent elements in two representative smartphone glass samples: non- and chemically tempered. APT has enabled sub-nanoscale analyses of alkali metals (Li, Na, K, and Ca) and this demonstrates that APT can be considered as an alternative technique for imaging the chemical distribution in glass for mobile applications.

**Key words:** atom probe tomography, chemically strengthened glass, ion exchange, ultrathin glass

## Introduction

Chemical strengthening of glass was initially proposed by Kistler (1962). This process involved replacing one of the constituents with an element of different atomic size and electronic polarizability while maintaining the structure of the pristine glass. Since then, extensive research and industrial efforts have been carried out to develop this approach for the mechanical strengthening of glass in a wide range of applications, including aircraft cockpits, digital dashboards, and passenger seat displays in automobiles, and hard disk drives for data storage (Gy, 2008). Most importantly, it is perceived as the best fabrication method to effectively strengthen ultrathin glass (UTG) sheets without influencing their optical properties and mass (Yuan et al., 2021). With a thickness below 100 $\mu$m, UTG is an increasingly popular display material that can be folded or rolled like a flexible polymer while protecting the screen (Tanaka, 2013). There are many promising applications for UTG ranging from wearable devices to solar cells and even flexible smartphones (SCHOTT, 2021). A recently available commercial flip phone already uses UTG with a thickness of 30 $\mu$m on its rigid display (SamsungDisplay, 2020). Moreover, UTGs with a thickness of ~5 $\mu$m have demonstrated good flexibility in micro-scale applications such as femtoliter nanofluidic valves (Kazoe et al., 2019) and diaphragm pressure transducers (Yalikun & Tanaka, 2017).

The manufacture of UTG usually involves the replacement of small ions (e.g., $Na^+$) by larger ones from an external ion source (e.g., $K^+$). It creates a compressive stress at the surface that improves mechanical strength, preventing the possible formation of micro/nano-cracks on the glass surface (Nordberg et al., 1964). However, if the ion-exchange process continues for a bulk glass, the surface compressive stress will increase, while the tensile stress inside the glass will rapidly increase. Additionally, a complete diffusion throughout the thickness could create severe internal-compressive stress, resulting in failure of the material (Shan et al., 2018; Terakado et al., 2020). Therefore, the depth of the ion-diffused layer (DOL), which is defined as the depth at which the residual stress is equal to zero, must be measured to ensure high-quality chemically strengthened glass. Generally, the DOL limitation for UTG is considered to be one-sixth of the glass thickness; hence, 830 nm would be the threshold depth for a 5-$\mu$m-thick UTG.

While the kinetics of the alkali ion interdiffusion process and chemical strengthening are well reported, the underlying atomic-scale compositional effect is less well understood, especially for UTG (Varshneya, 2010). This is due to the limitations of in-depth chemical characterization instruments that offer site-specific analyses. Accordingly, most research still relies on spectroscopy techniques or the nominal weight compositions from powder-melting synthesis (Farah et al., 2014; Wang et al., 2014; Kim et al., 2021). Herein, we assess the performance of atom probe tomography (APT; Gault et al., 2021) in a systematic comparison with more conventional chemical analysis tools on an aluminosilicate tempered glass and correlate it with increases in glass hardness. We also discuss the strength and weaknesses of these selected techniques and demonstrate the complementarity offered by APT that provides spatially resolved distribution of alkali-(earth) elements at the subnanometer level, including light and trace elements.

## Materials and Methods

### Materials

We selected an aluminosilicate glass with an initial thickness of 750 $\mu$m that is used for a commercial mobile display. The

**Received:** March 30, 2022. **Revised:** February 16, 2023. **Accepted:** March 4, 2023

material was supplied by a private company. Two glass samples were prepared; one without any further chemical or heat treatment (Glass_0), and one subjected to ion-exchange treatment by using an industrial-scale furnace that allowed the treatment of a series of samples (Glass_1).

### Ion Exchange

In the ion-exchange process, the time that the pristine sample was submerged into the alkaline solution was calculated based on the diffusion law. Usually, a batch temperature of below 460°C and a processing duration of <24 h are recommended (Bartholomew & Garfinkel, 1980). A potassium nitrate ($KNO_3$) salt bath was prepared by heating an industrial source (>99.9%) of $KNO_3$ to ~460°C. The sample (Glass_1) was then submerged into the bath in the furnace for 1 h to achieve an equilibrium state.

### Mechanical Testing

Two $2 \times 2$ cm$^2$ samples were prepared from 750 $\mu$m thickness blank samples: Glass_0 and _1 glasses. Nano-indentations tests were done using a Berkovich indenter with an apex semi-angle of 65° and with a constant indenter load of 9 mN. One hundred indentations were made on each specimen and a distance of 5 $\mu$m was kept between the centers of each indentation.

### Characterization

The Glass_0 and Glass_1 samples were characterized with respect to their composition, structure, and vibration spectrum using inductively coupled plasma optical-emission spectroscopy (ICP-OES, Agilent 5800) and Raman spectroscopy (WiTec: Alpha300) in the range of 200–2,000/cm with a green laser source (wavelength: 532 nm).

Scanning electron microscope (SEM)-energy dispersive X-ray spectroscopy (EDS) elemental analysis (FEI Helios Nanolab 600i) was performed on the Au-coated glass samples at 30 kV accelerating voltage and 2.4 nA current.

The surface region was prepared into a series of APT specimens by using a site-specific preparation approach using a Ga-focused ion-beam (FIB)/SEM (FEI Helios Nanolab 600i) (Fig. 1; Thompson et al., 2007). The APT analyses were performed on both samples by using local electrode atom probes [CAMECA reflectron-fitted LEAP 5000 (XR) and straight-flight-path LEAP 5000 (XS) systems] in pulsed UV laser mode at a detection rate of 1%, a laser-pulse energy of 90 pJ, and a pulse frequency of 125 kHz. The specimen temperature was set to 60 K during the analyses. The data reconstruction and analyses were performed using the commercial software Imago visualization and analysis system standard (IVAS) 3.8.2 developed by CAMECA Instruments. It should be noted that a low composition below 0.5 at% Ga originating from the focused-ion beam preparation was detected. However, when the Xe FIB system (Helios plasma-FIB Thermo-Fisher) was used for the APT specimen preparation a negligible amount of Xe was detected in the glass specimen.

## Results and Discussion

### Mechanical Testing

Glass_0 and Glass_1 (2 h of chemical treatment) are displayed in Figure 2a. Nano-indentations were performed on both samples, where the hardness of Glass_1 exhibited a 7.3% higher value than that of Glass_0, which was expected (Fig. 2b). Although Raman spectroscopy is often used to identify the chemical structure in tempered glass, in our case, despite a sufficient amount of time for a complete ion-exchange process, no clear indication of peak shifts or intensification between

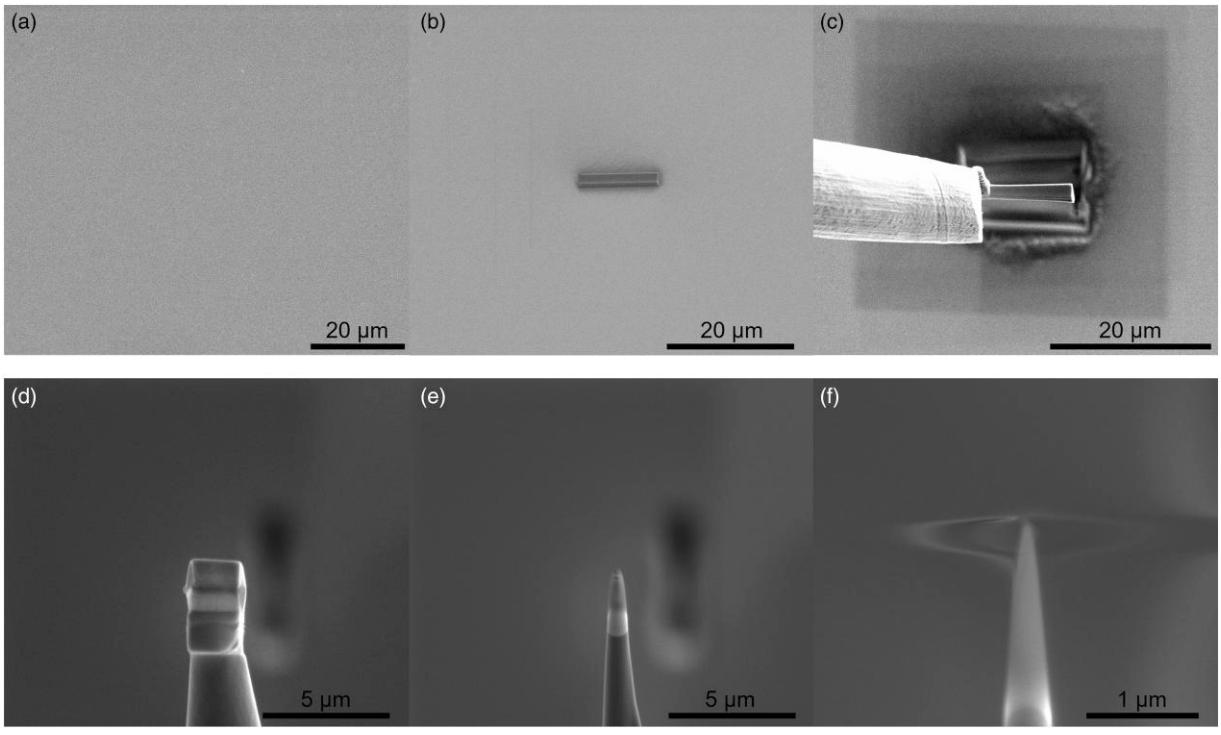


**Fig. 1.** APT specimen preparation: (**a**) surface of a Glass_0 sample, (**b**) FIB Pt-C coating, (**c**) lift-out process using an omniprobe, (**d**) welding on a Si micro-post, (**e**) annular milling process, and (**f**) final needle-like APT specimen.

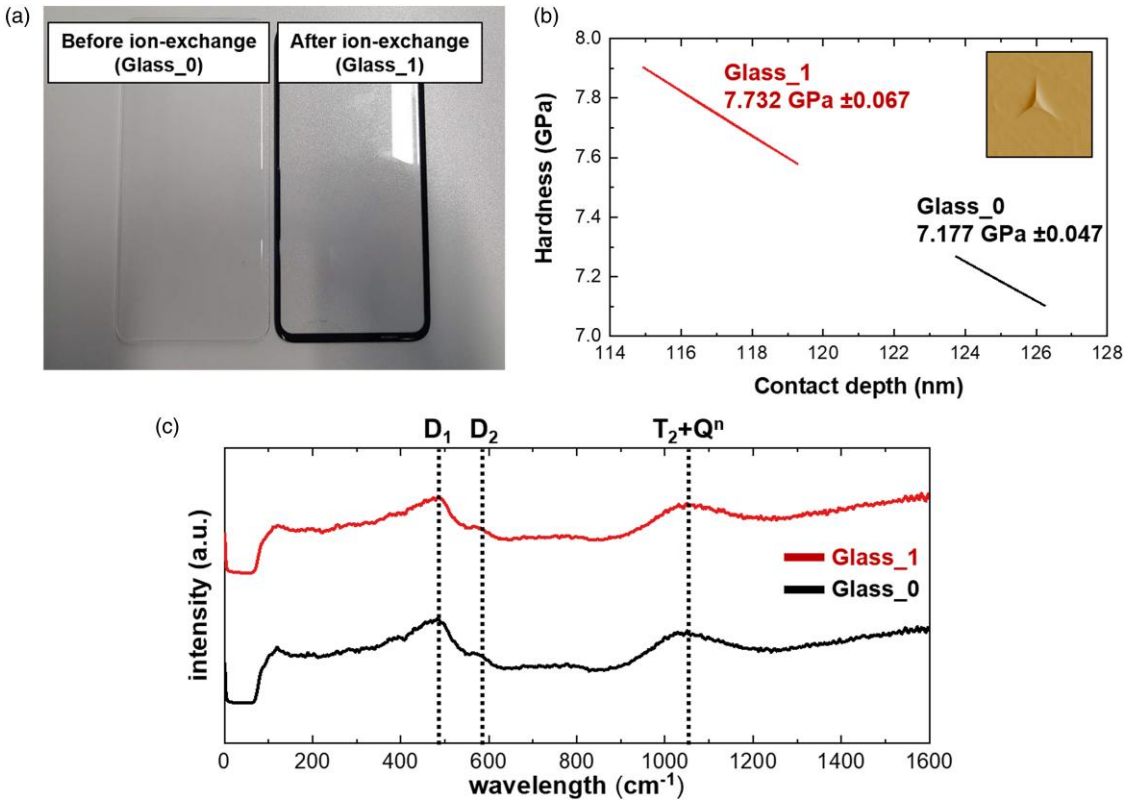


**Fig. 2.** (**a**) As-received glass and chemically tempered glass. The black film around the tempered glass (Glass_1) is to protect the edge panel from scratches during mobile phone manufacturing. (**b**) Vickers hardness (LECO M-400) tests. (**c**) Raman spectroscopy (WiTec: Alpha300R) results.

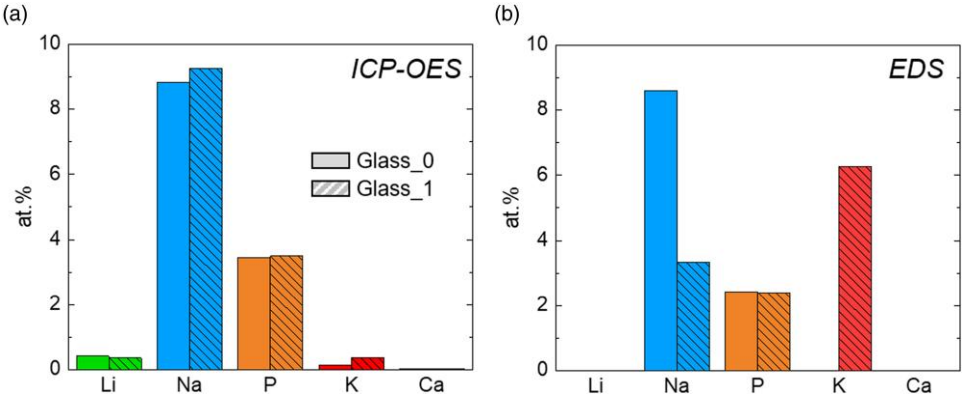


**Fig. 3.** Composition comparison plots of Li, Na, P, K, and Ca for Glass_0 and Glass_1 from (**a**) ICP-OES and (**b**) SEM-EDS.

samples was measured (Fig. 2c). Typically, a higher K content in silicate glass results in a shift of the Si–O peak toward 1,110/cm (Calahoo et al., 2016). The broad Raman peak at 1,050/cm corresponded with the mixed signal of the stretching $T_2$ vibrational mode of Al/Si–$O_4$ tetrahedra and stretching Al/Si–O of the different Q-bands units (Mysen, 1990; Malfait et al., 2008; Le Losq et al., 2014). The peaks at $D_1$ (480/cm) and $D_2$ (580/cm) peaks corresponded to symmetric stretching of O atoms in the four and three-membered tetrahedral rings, respectively (Le Losq et al., 2014; Terakado et al., 2020).

## Bulk Characterization

ICP-OES is commonly used for chemical analysis of tempered glass (Schenk & Almirall, 2012; Calahoo et al., 2016). Here, the dissolved liquid glass is heated with plasma emitting light which is then measured with the spectrometry. After the exchange process, an increase in K content was observed. However, the overestimation of the Na content after the exchange disagreed with the expected result (Fig. 3a, Table 1). A possible explanation for this could be the introduction of Na during the preparation of the specimens. Each glass display was crushed into a powder with a mortar and pestle, followed by dissolution with hydrofluoric acid. Moreover, the mortar and pestle constituent element (e.g., Zr) was also detected implying the possible introduction of impurities during sample preparation, although this was not detected when using the other analytical techniques.

The SEM-EDS elemental analysis is commonly employed for analyzing the chemical composition of glass (Erdem et al.,

**Table 1.** Atomic Composition of Elements for Glass_0 and Glass_1 Measured by ICP-OES, SEM-EDS, APT-HR, and APT-XS. Please note that the oxygen content from ICP-OES was calculated by normalizing from the detected composition.

| | | | | | | | | | Impurities from Sample Preparation | | | |
|---|---|---|---|---|---|---|---|---|---|---|---|---|
| At% | O | Si | Al | Li | Na | P | K | Ca | Ga | Au | Zr | C |
| *Glass_0* | | | | | | | | | | | | |
| ICP-OES | 36.96 | 34.66 | 15.26 | 0.42 | 8.82 | 3.46 | 0.13 | 0.032 | — | — | 0.25 | 0.01 |
| SEM-EDS | 34.14 | 34.95 | 16.68 | — | 8.59 | 2.43 | — | — | — | 3.21 | — | — |
| APT_XR | 56.47 | 21.95 | 11.52 | 4.87 | 3.25 | 1.85 | 0.017 | 0.023 | 0.048 | — | — | — |
| APT_XS | 55.61 | 20.81 | 12.72 | 4.47 | 4.43 | 1.46 | 0.015 | 0.027 | 0.47 | — | — | — |
| *Glass_1* | | | | | | | | | | | | |
| ICP-OES | 36.95 | 34.36 | 14.99 | 0.37 | 9.26 | 3.5 | 0.37 | 0.028 | — | — | 0.23 | 0.01 |
| SEM-EDS | 42.07 | 30.35 | 14.42 | — | 3.34 | 2.4 | 6.26 | — | — | 1.15 | — | — |
| APT_XR | 57.15 | 22.86 | 12.31 | 1.97 | 1.96 | 1.76 | 1.69 | 0.05 | 0.24 | — | — | — |
| APT_XS | 55.95 | 21.53 | 14.03 | 2.68 | 2.1 | 1.37 | 2.24 | 0.056 | 0.054 | — | — | — |

2017; Fourmentin et al., 2021). With SEM-EDS, a depth resolution of ~2 $\mu$m is possible, which is typically sufficient for near-surface chemistry analysis (EDAX, 2020). Figure 4 displays the surface SEM images and EDS spectra of Glass_0 and Glass_1. The atomic fraction of the detected trace elements (Na, P, and K) is plotted in Figure 3b. The decrease in Na after the ion-exchange process indicated that Na was replaced by K in the analyzed region. However, no information regarding other elements (Li and Ca) was obtained due to the elemental detection limit for the trace amount (<0.5 wt%), particularly for light elements (Leng, 2013). Unfortunately, this representative result might not provide sufficient details for advancing our understanding of the chemical-exchange effect.

## Atom Probe Tomography

We performed APT to evaluate the composition and distributions of elements in both samples. Moreover, three APT measurements were performed on each sample and we obtained total counts of 41.2 and 53.7 M ions before and after chemically tempering the samples, respectively. These were then used for the chemical compositional analysis. Unlike X-ray-based spectroscopy or other bulk-mass spectrometry techniques, APT does not require corrections by relative sensitivity factors, which can vary by orders of magnitude depending on the considered element. Moreover, despite the known issues when detecting substances [e.g., oxygen (Saxey, 2011; Gault et al., 2016; Zanuttini et al., 2017) and alkalis (Greiwe et al., 2014; Lu et al., 2017)] in oxides, APT has the potential to provide local analysis with chemical sensitivity in combination with a subnanometer spatial resolution for detecting local deviations in composition (Gin et al., 2013; Wang et al., 2016; Lu et al., 2017).

Typically, different acquisition parameters (e.g., base temperature and laser-pulse energy) can affect APT performance, including background levels and eventually mass and spatial resolutions. Particularly, in the case of poor- or non-conductive materials (such as glass), the measurement parameters require careful optimization (see Fig. 5). The laser parameters were swept every 2.5 million ions for the glass specimens. In general, pulsing at a low laser repetition rate requires relatively more time to collect a sufficient number of ions to ensure statistically relevant analyses, whereas field evaporation at high laser-pulse energy often results in the development of thermal tails. Accordingly, 125 kHz and 90 pJ were selected as the optimal parameter conditions in the LEAP 5000XR system.

Examples of mass spectra obtained from both instruments are shown in Figures 6a and 6b. The former exhibited a detection efficiency of ~80%, compared with the latter with only ~50%. In contrast, the XR system achieved a higher mass resolution, as the reflectron enabled longer flight times, resulting in better separation of the mass peaks. For instance, in the XR system, a clear peak at 15.5 Da corresponding to $^{31}P^{2+}$ ion was detected with the full width half maximum of 0.05244 (insets in Fig. 6). In comparison, the FWHW of the $^{31}P^{2+}$ peak in the XS system was 0.15732, which was three times higher than that of the XR system. No significant difference in overall atomic composition was revealed between the two instruments (Table 1). However, a noticeable peak at 15.66 Da in the HR system (corresponding to $PO^{3+}$) was detected, which was not observed in the XS mass spectra. Therefore, for a more accurate analysis, we used the HR system for detailed chemical analysis of the acquired mass spectrum.

As mentioned previously, quantification by APT for a ceramic sample is challenging. The data set from Glass_2 in the LEAP 5000 XS was further analyzed to investigate the multiplicity of the detected ions to determine whether additional chemical information could be retrieved from the otherwise un-identified ions. In Figure 7a, the correlation histogram of the multiple-ion events demonstrates that there was continuous field evaporation of complex oxygen-containing molecular ions caused by the electrostatic field. In other words, this was not triggered by the temperature increase associated with the laser pulse (which can be considered DC evaporation) or by the very long delay following the thermal pulse. These ions were the main contributors to the high background levels. From the origin, there were parabolic trails that indicated ion evaporation was induced by a standing DC field without the absence of pulsing (Saxey, 2011). Moreover, despite the strong and clearly discernible peaks throughout the mass-to-charge spectrum of the tempered state, the background still represents a large portion (30%). In addition, the single ($M = 1$) spectrum had a slightly different distribution to the multiple ($M > 1$) spectrum (Fig. 7b). This difference could be attributed to a distinct component corresponding to a higher fraction of DC evaporation events. This phenomenon was discussed previously by Yao et al. (2010, 2013). Nevertheless, our interest was primarily in the detection of alkali ion species that do not seem to be affected as much compared with Al, Si, and mostly O ions. This could be related to their high electropositivity, which renders them less prone to forming molecular ions under intense positive electric fields.

Figure 8 displays the overall reconstructed 3D atom maps of Glass_0 (up) and Glass_1 (down). Here, major elements (Al, Si, and O), minor elements (P, Li, Na, and K), and a trace

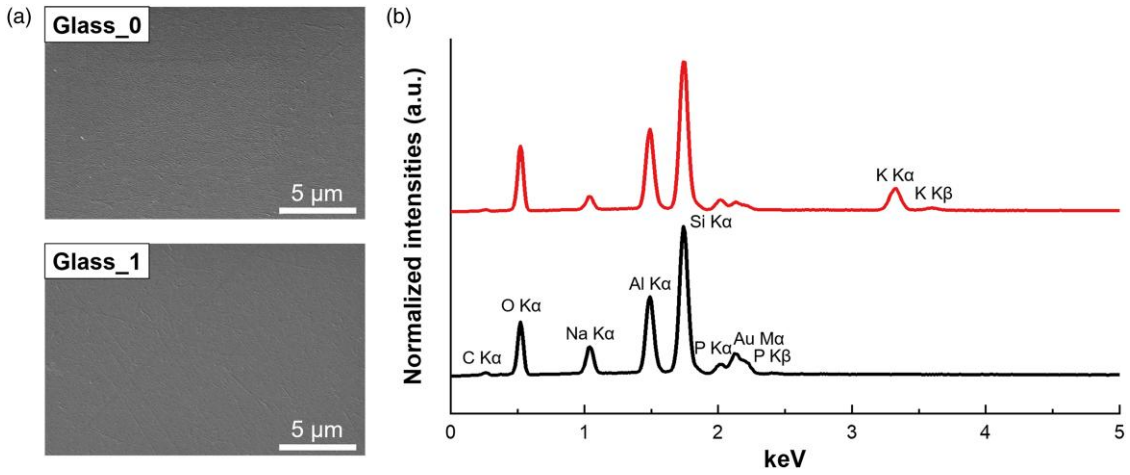


**Fig. 4.** (**a**) SEM surface images of Au-coated Glass_0 and Glass_1 samples, and (**b**) corresponding SEM-EDS spectra. A thin layer of Au was coated prior to the EDS-SEM measurements; hence, the Au signal was not from the sample.

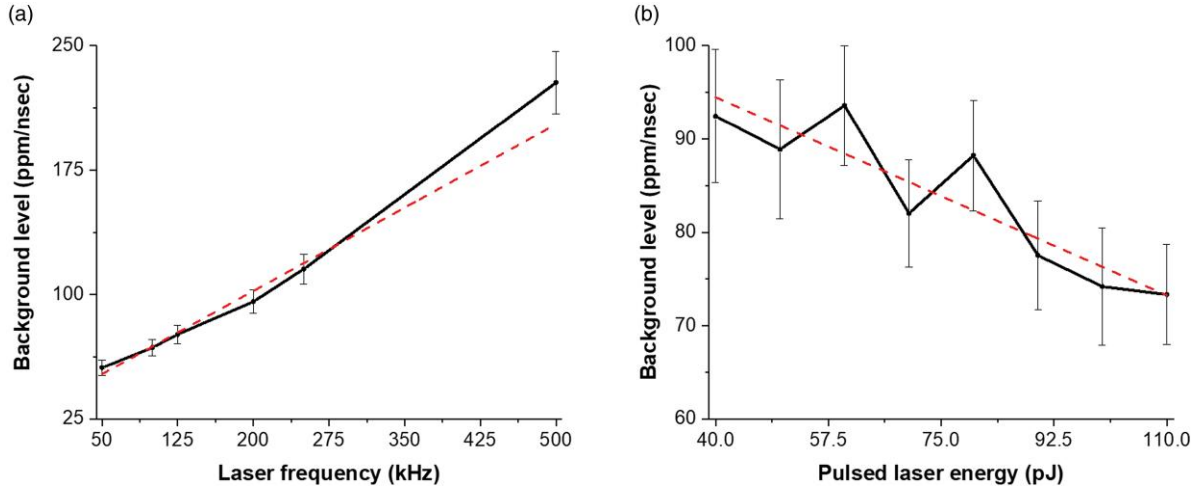


**Fig. 5.** Background levels versus (**a**) laser frequency and (**b**) pulsed-laser energy.

element (Ca, not shown in the atom maps) were detected. The mass spectrum in Figure 6c can be referenced for the element species. All the elements were visually homogeneously distributed and no enrichment or depletion are observed. To investigate the chemistry and structure further, the inner regions of the atom maps were extracted as shown in Figure 9a: Glass_0 (right) and Glass_1 (left).

After the ion exchange, different content levels of alkali elements such as Li, Na, and K were detected in the Glass_1 sample. The distributions of the alkali ions were assessed by using a nearest-neighbor analysis, and they appeared comparable with random distribution (Stephenson et al., 2007; Shariq et al., 2012) (Figs. 9b, 9c). For a quantitative assessment of the randomness analysis, the Pearson coefficient ($\mu$) was measured for each alkali element. Here, all the coefficients are near-zero values ($\mu_{Li} = 0.0132$, $\mu_{Na} = 0.0983$, $\mu_{K} = 0.103$) suggesting that the alkali ions were randomly distributed in the glass. The levels of $Li^+$ and $Na^+$ decreased by factors of 2.5 and 1.6, respectively, whereas the content of $K^+$ increased by up to 1.7 at%. Interestingly, the reduction in $Li^+$ concentration was larger than for $Na^+$. This can be simply explained by the higher diffusivity with respect to ion radii: $Li^+$ has the smallest size of 78 p.m., whereas $Na^+$ and $K^+$ have the size of 98 and 133 p.m., respectively. The $Li^+$–$K^+$ ion replacement would have a greater size mismatch; hence, a greater compressive stress was formed compared with the $Na^+$–$K^+$ exchange.

For the Li-doped amorphous silicate, Li electromigration was observed and Li ions continuously moved toward the specimen apex during the field evaporation process (Greiwe et al., 2014). In contrast, despite the long measurements (>5 M ions) in the aluminosilicate glass, no migration of Li or other elements was observed (see Figs. 8, 9c). This phenomenon could be due to difference in Li-ion transport characteristics between the amorphous and glass structures and thermal interaction between the laser and the specimen. The atomic ratio of Si to Al for both types of glass was ~2, indicating that the molecular ratio of $Al_2O_3$ to $SiO_2$ compounds was 1:1. This agrees with the 1:1 ratio of $Al_2O_3$ and $SiO_2$ that was measured with other analytical instruments, as summarized in Figure 10a.

In addition, P and Ca were also detected, with 1.85 at% and 230 appm, respectively, in Glass_1. $PO_x$ in aluminosilicate is known to increase compressive stresses, and any increase in concentration can effectively promote $Na^+$ and $K^+$ inter-diffusivity (Mysen, 1998; Zeng et al., 2016). Nevertheless, the $PO_x$ in

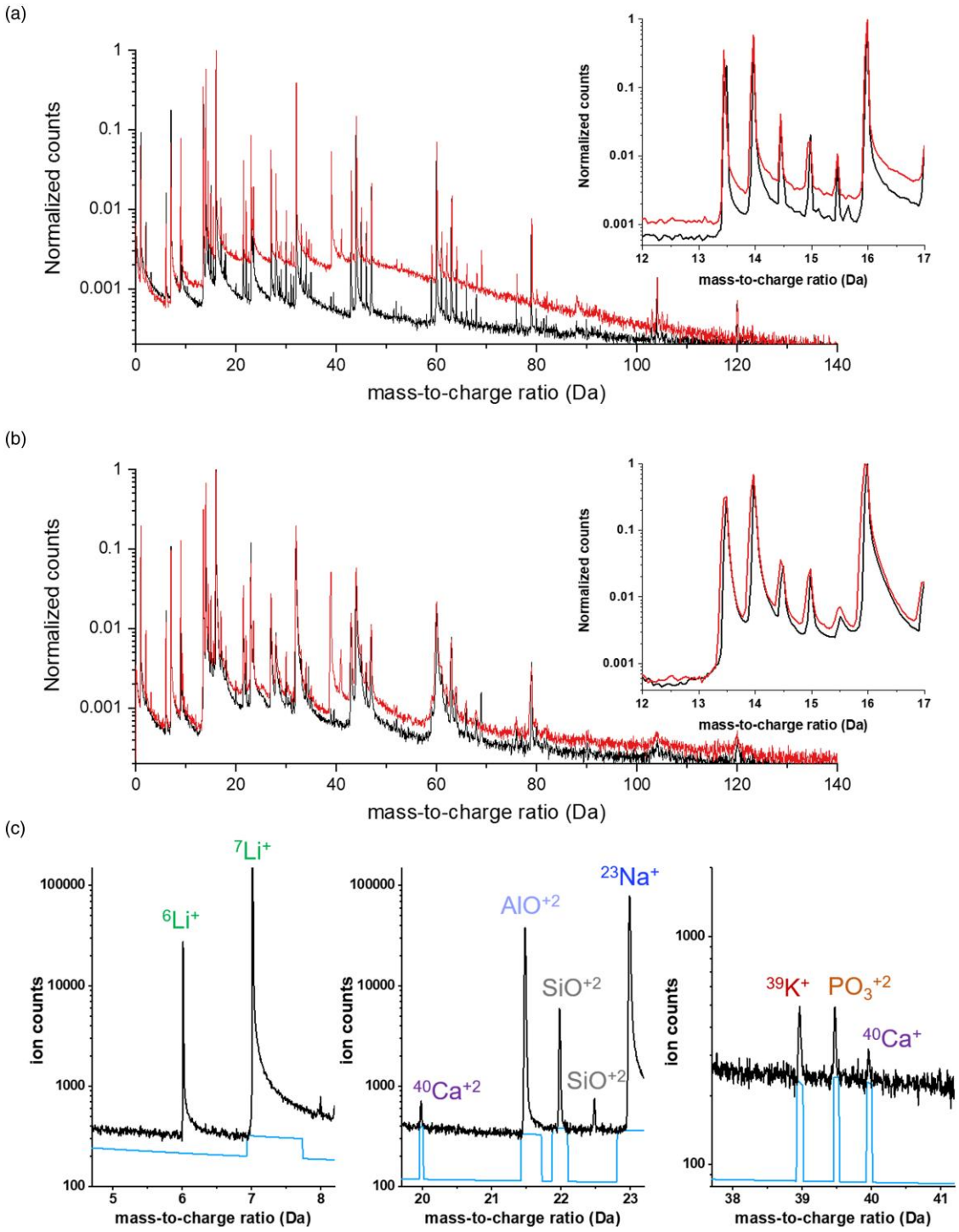


**Fig. 6.** Normalized mass spectra of Glass_0 (black) and Glass_1 (red) samples from (**a**) 5000 HR and (**b**) 5000 XS atom probe instruments. Insets display the extracted mass spectrum regions at 12–17 Da on each data set. (**c**) Three different ion-count mass spectrum ranges for each alkali species. The actual background level is plotted with a blue line.

aluminosilicate is susceptible to water or moisture and can be leached even at room temperature (Tošić et al., 2013).

## General Discussion

In the chemical-tempered glass industry, the presence of Ca cations in concentrations as low as 10 ppm in the ion-exchange $KNO_3$ bath can cause major problems (Sglavo, 2015). This is because $Ca^{2+}$ penetrates the silicate compound surface, inhibiting the $Na^+$–$K^+$ exchange and preventing the generation of the necessary compressive stress (Xiangchen et al., 1986; Sglavo et al., 2017). Given that Ca has an ionic radius (100 pm) very similar to $Na^+$ and smaller than $K^+$, replacement with $Na^+$ is favorable on the glass surface. Although a high purity level of molten $KNO_3$ was used, the Ca content in the glass after the chemical tempering increased by a factor of 2. A comparison of minor elements compositions before and after chemically tempered glasses is summarized in Figure 10b.

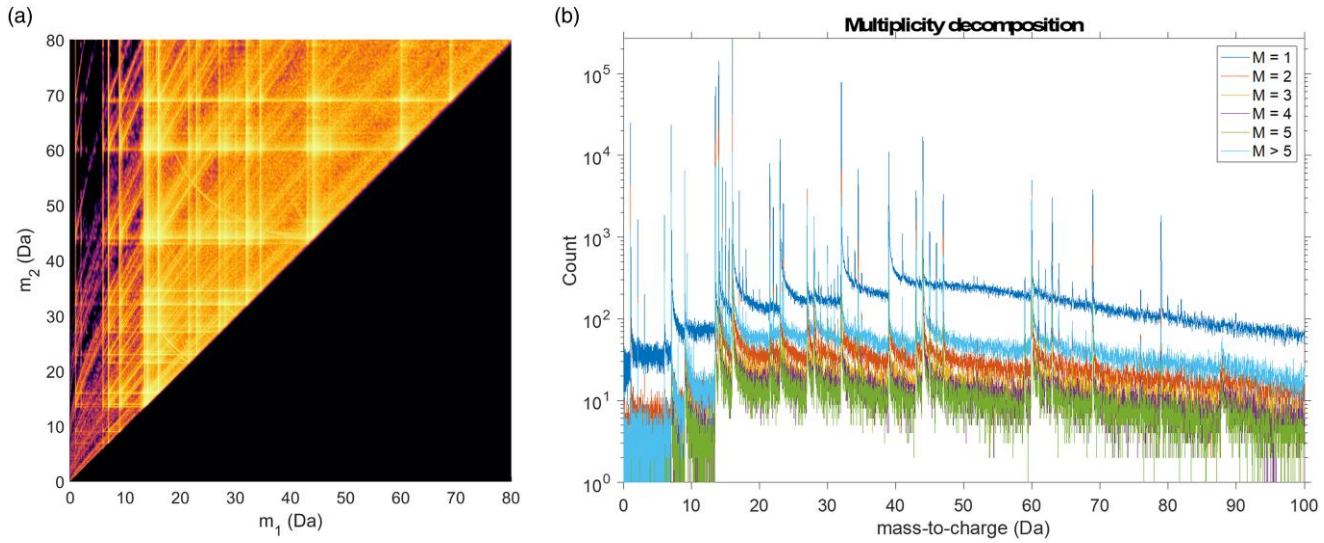


**Fig. 7.** An issue in the mass spectroscopy of oxide materials arises from evaporation uncorrelated with the laser pulse. (**a**) Correlation histogram of multiple hits. (**b**) Multiplicity decomposition of single, double, triple, quadruple, and quintuple hits.

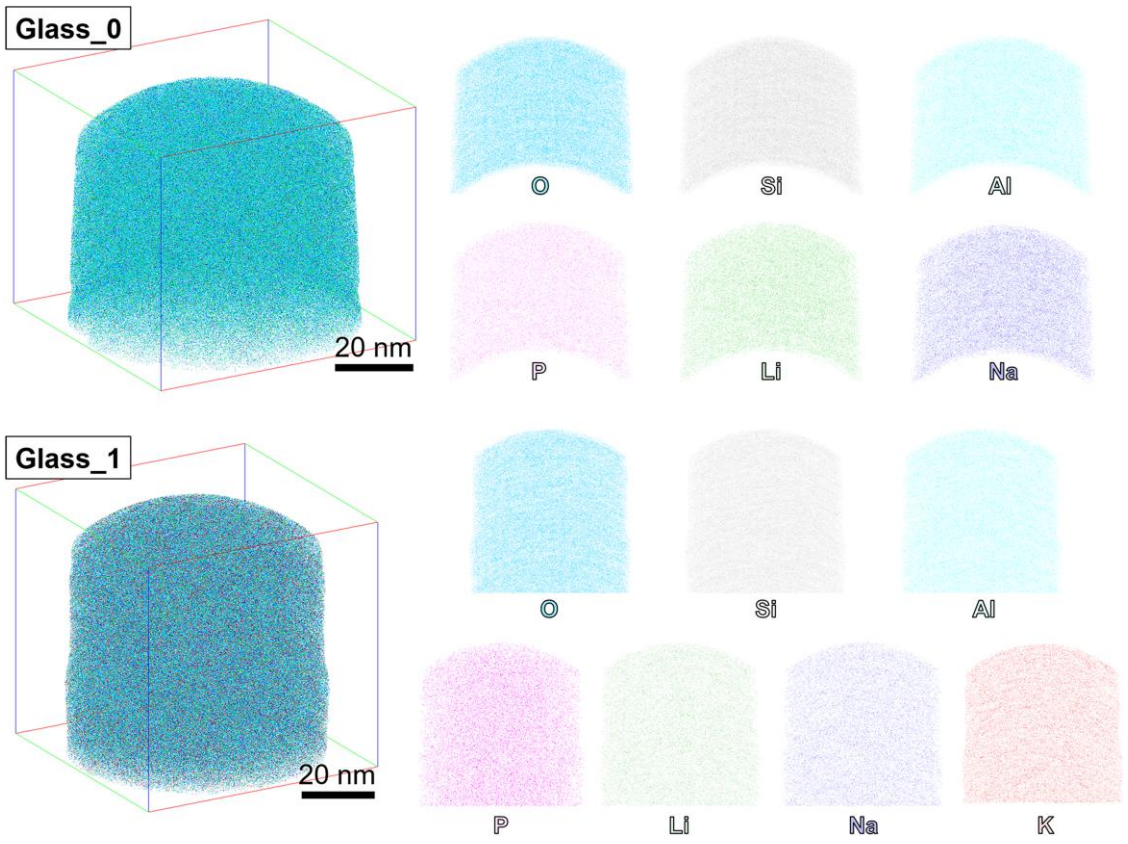


**Fig. 8.** 3D atom maps of (top) Glass_0 and (bottom) Glass_1 samples. The APT measurements on semiconductor and ceramic materials exhibited a consistent deficiency in O, which could not be removed by parameter optimization. It is postulated that the fragmentation of evaporated molecular oxide ions could play a role in producing neutral O atoms that cannot cascade the signals on the analysis detector. Nevertheless, in this work, the APT results exhibited a high accuracy of O content compared with other analytical measurements.

When alkali-(earth) ions are exchanged in the network glass, the charge neutrality must be preserved. However, here more Li and Na ions were lost than replaced by K and Ca ions. Incorrect peak assignment or peak overlapping of alkali species from the acquired mass spectra are unlikely to occur as the ions evaporates in the single-charge state (Kingham, 1982; Kim et al., 2022*a*, 2022*b*; Yoo et al., 2022). Hence, charge neutrality approximation was adopted in the ion-exchange glass for modeling purposes (Garfinkel, 1968) and was assumed for simplification. However, this approximation considers only two types of ions with the same valence state (indigenous and modifier cations) in one-to-one

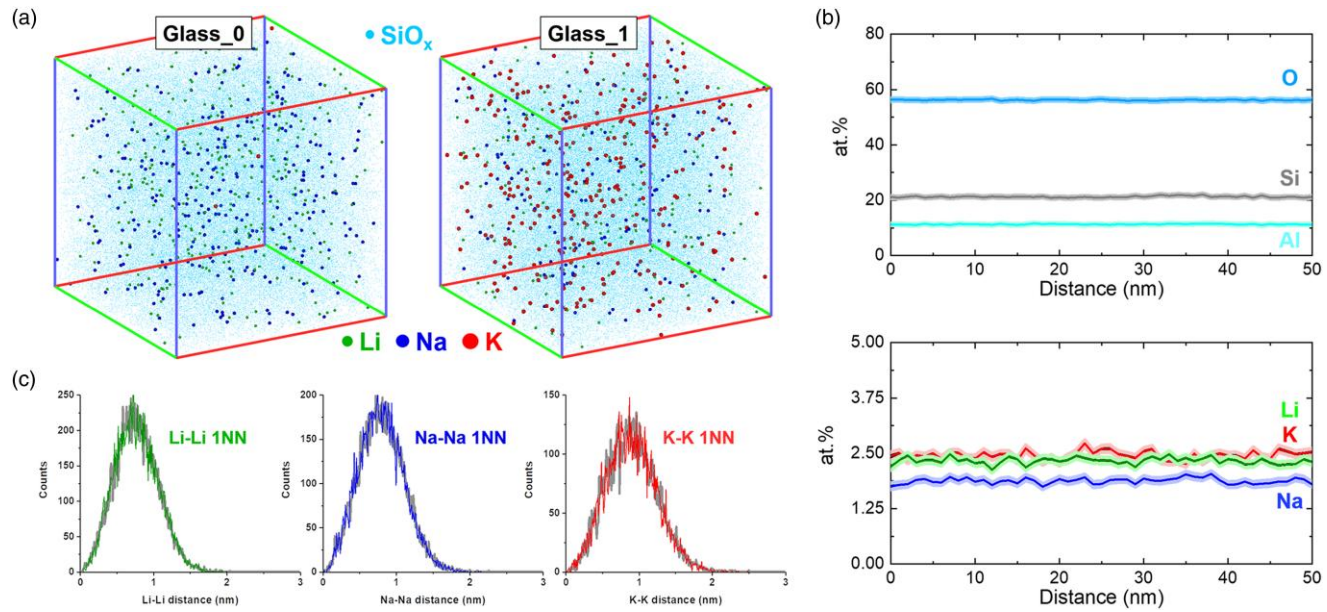


**Fig. 9.** (**a**) 3D reconstructed atom maps ($35 \times 35 \times 35$ nm$^3$) of the Glass_0 and Glass_1. Light blue, green, blue, and red dots represent Li, Na, and K atoms in the SiOx complexes, respectively, while P and Ca atoms are not shown. Each cuboidal ROI was extracted from the overall atom map displayed in Fig. 8. (**b**) 1D atomic compositional profile of the Glass_1 along the measurement direction ($\phi$15 nm $\times$ 50 nm$^3$ and bin width of 1 nm). The standard error values were calculated from the binomial distribution. (**c**) Experimental and random (gray) alkali-alkali elements nearest-neighbor (1NN) distribution.

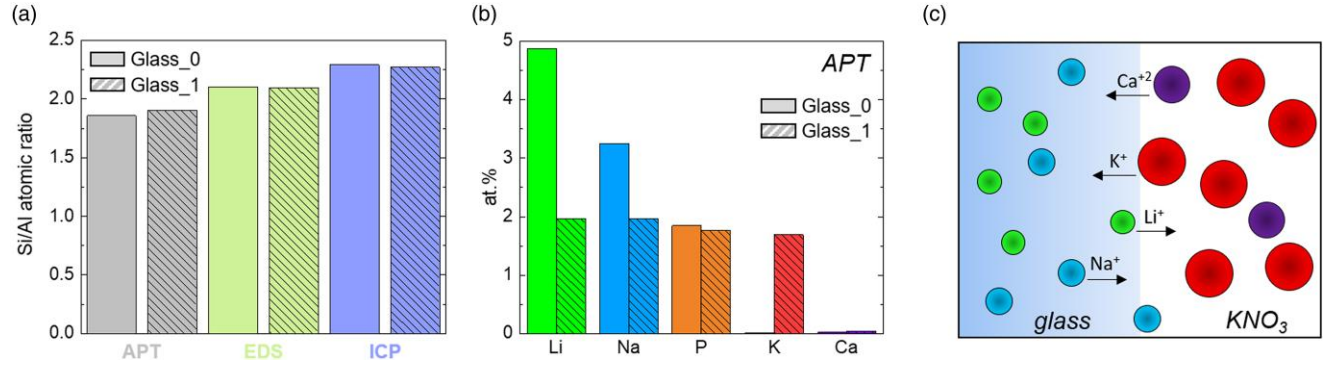


**Fig. 10.** (**a**) Si/Al ratio of Glass_0 and Glass_1 from different analytical instruments: APT, SEM-EDS, and ICP-OES. Composition comparison plots of Li, Na, P, K, and Ca for Glass_0 and Glass_1 from APT. (**c**) Schematic illustration of alkali (earth) ion diffusion during glass tempering.

direct exchanges. Moreover, there are other factors can be considered.

### *Alumina (Al–O)*

The material studied herein is an aluminosilicate glass, where the alumina serves as a glass former and generally improves durability. Moreover, alumina generally plays an important role in ion exchange, since it provides a strong network and acts as a charge balancer. The structure of aluminum ions depends on the glass composition (Yan et al., 1996). For example, when the alkali-oxide (e.g., $Na_2$-O) content is higher than alumina, all alumina is found in tetrahedral coordination with compensating the alkali ions charges. In constrast, when the alumina content is higher, alkali-oxide changes to an s divalent Na-O structure varying the degree of tetrahedral aluminum. As a result, depending on the alkali element content in the glass, this results in the formation of five- and sixfold coordinated aluminum ions (Xiang et al., 2013), while retaining its glass network. This implies that no one-to-one exchanges are possible during the chemical tempering process.

### *Hydrogen*

Hydrogen or hydronium ions could also affect the glass structure and contribute to charge neutralization. The diffusion and permeability of hydrogen in silicate glass have been extensively studied (Williams & Ferguson, 1922), where it was revealed that above 300°C, silica glass is permeable to hydrogen (the operating temperature for the chemical process of this work was >400°C). Moreover, Landford et al. observed a hydrogen–sodium exchange in soda-lime glass (Lanford et al., 1979; Schnatter et al., 1988), and Isard et al. investigated Na–H ion exchange in aluminosilicate glass catalyzed by sulfur oxides at room temperature (Douglas & Isard, 1949). In recent studies, the field-assisted injection of hydrogen from the atmosphere into the glass was demonstrated to replace the indigenous ions (Na, K, and Ca) with hydrogen (Oven, 2021*a*, 2021*b*). They used a modified charge neutrality

approximation by adding a concentration of H into the model, rending their system more accurate.

Ultimately, as thinner UTG will open a wider range of technological applications within electronics, site-specific chemical information must first be provided to allow a better understanding of the material and its mechanical and functional behaviors to avoid any mis-interpretations. For instance, the spectroscopy results exhibited no/less signal of the Li and the alkali-earth element Ca. Herein, we demonstrate the importance of using accurate chemical analysis on a commercial glass before and after strengthening by ion exchange. As presented in the summarized schematic diagram (Fig. 10c), $Li^+$ and $Na^+$ diffused from the glass to the $KNO_3$ bath, where $K^+$ and impurity $Ca^{2+}$ diffused into the surface.

## Conclusions

In this paper, we reported on a comparative study of spectroscopy and APT in the atomic-scale mapping of alkali ions in non- and ion-exchanged glass. We demonstrated that APT is superior to commonly used spectroscopy techniques in terms of both spatial resolution and quantification. In addition, direct-flight and reflectron-flight atom probe systems were compared and no significant difference was observed in terms of composition. In UTG technology, it is very important to quantify and image the exchanged alkali ions to simultaneously increase hardness and flexibility. Therefore, site-specific mass spectrometry techniques (such as APT) are required to understand the direct relationship between the chemistry and the mechanical properties of such types of glass.

## Acknowledgments

B.G., L.T.S., and S.-H.K. acknowledge financial support from the ERC-CoG-SHINE-771602. The authors appreciate Heidi Bögershausen, Petra Ebbinghaus, and Daniel Kurz for Vickers hardness, Raman spectroscopy, ICP-OES measurements. They also thank Uwe Tezins, Christian Broß, and Andreas Sturm for providing us access to the FIB and APT facilities at the MPIE. Dr Dong-Hyun Lee is gratefully acknowledged for the discussions.

## Financial Support

The current study hasn't received any fund from any organizations or institutions.

## Conflict of Interest

The authors declare that they have no competing interest.

## References

Bartholomew RF & Garfinkel HM (1980). Chapter 6-Chemical strengthening of glass. In *Glass Science and Technology: Elasticity and Strength in Glasses*, **vol. 5**, Uhlmann DR & Kreidl NJBT-GS (Eds.), pp. 217–270. New York (NY): Academic Press.

Calahoo C, Zwanziger JW & Butler IS (2016). Mechanical–structural investigation of ion-exchanged lithium silicate glass using micro-Raman spectroscopy. *J Phys Chem C* **120**, 7213–7232. https://doi.org/10.1021/acs.jpcc.6b01720

Douglas R & Isard J (1949). The action of water and of sulfur dioxide on glass surfaces. *J Soc Glass Technol* **33**, 289–335.

EDAX (2020). Optimizing spatial resolution for EDS analysis. *EDAX insight*.

Erdem İ, Guldiren D & Aydin S (2017). Chemical tempering of soda lime silicate glasses by ion exchange process for the improvement of surface and bulk mechanical strength. *J Non-Cryst Solids* **473**, 170–178. https://doi.org/10.1016/j.jnoncrysol.2017.08.010

Farah K, Hosni F, Mejri A, Boizot B, Hamzaoui AH & Ben Ouada H (2014). Effect of gamma rays absorbed doses and heat treatment on the optical absorption spectra of silver ion-exchanged silicate glass. *Nucl Instrum Methods Phys Res B* **323**, 36–41. https://doi.org/10.1016/j.nimb.2014.01.019

Fourmentin C, Zhang X-H, Lavanant E, Pain T, Rozé M, Guimond Y, Gouttefangeas F & Calvez L (2021). IR GRIN lenses prepared by ionic exchange in chalcohalide glasses. *Sci Rep* **11**, 11081. https://doi.org/10.1038/s41598-021-90626-4

Garfinkel HM (1968). Ion-exchange equilibriums between glass and molten salts. *J Phys Chem* **72**, 4175–4181. https://doi.org/10.1021/j100858a040

Gault B, Chiaramonti A, Cojocaru-Mirédin O, Stender P, Dubosq R, Freysoldt C, Makineni SK, Li T, Moody M & Cairney JM (2021). Atom probe tomography. *Nat Rev Methods Primers* **1**, 51.

Gault B, Saxey DW, Ashton MW, Sinnott SB, Chiaramonti AN, Moody MP & Schreiber DK (2016). Behavior of molecules and molecular ions near a field emitter. *New J Phys* **18**, 33031. https://doi.org/10.1088/1367-2630/18/3/033031

Gin S, Ryan JV, Schreiber DK, Neeway J & Cabié M (2013). Contribution of atom-probe tomography to a better understanding of glass alteration mechanisms: Application to a nuclear glass specimen altered 25 years in a granitic environment. *Chem Geol* **349–350**, 99–109. https://doi.org/10.1016/j.chemgeo.2013.04.001

Greiwe G-H, Balogh Z & Schmitz G (2014). Atom probe tomography of lithium-doped network glasses. *Ultramicroscopy* **141**, 51–55. https://doi.org/10.1016/j.ultramic.2014.03.007

Gy R (2008). Ion exchange for glass strengthening. *Mater Sci Eng B* **149**, 159–165. https://doi.org/10.1016/j.mseb.2007.11.029

Kazoe Y, Pihosh Y, Takahashi H, Ohyama T, Sano H, Morikawa K, Mawatari K & Kitamori T (2019). Femtoliter nanofluidic valve utilizing glass deformation. *Lab Chip* **19**, 1686–1694. https://doi.org/10.1039/C8LC01340C

Kim S-H, Antonov S, Zhou X, Stephenson LT, Jung C, El-Zoka AA, Schreiber DK, Conroy M & Gault B (2022*a*). Atom probe analysis of electrode materials for li-ion batteries: Challenges and ways forward. *J Mater Chem A* **10**, 4926–4935. https://doi.org/10.1039/D1TA10050E

Kim S-H, Yoo S-H, Chakraborty P, Jeong J, Lim J, El-Zoka AA, Zhou X, Stephenson LT, Hickel T, Neugebauer J, Scheu C, Todorova M & Gault B (2022*b*). Understanding alkali contamination in colloidal nanomaterials to unlock grain boundary impurity engineering. *J Am Chem Soc* **144**, 987–994. https://doi.org/10.1021/jacs.1c11680

Kim SW, Im H-T, Lee JE, Kim HS, Kim JH & Hwang J (2021). Physical properties of chemically strengthened thin glass prepared by the spray method using an original KNO3–Al2O3 slurry. *Mater Chem Phys* **259**, 123942. https://doi.org/10.1016/j.matchemphys.2020.123942

Kingham DR (1982). The post-ionization of field evaporated ions: A theoretical explanation of multiple charge states. *Surf Sci* **116**, 273–301. https://doi.org/10.1016/0039-6028(82)90434-4

Kistler SS (1962). Stresses in glass produced by nonuniform exchange of monovalent ions. *J Am Ceram Soc* **45**, 59–68. https://doi.org/10.1111/j.1151-2916.1962.tb11081.x

Lanford WA, Davis K, Lamarche P, Laursen T, Groleau R & Doremus RH (1979). Hydration of soda-lime glass. *J Non-Crystal Solids* **33**, 249–266. https://doi.org/10.1016/0022-3093(79)90053-X

Le Losq C, Neuville DR, Florian P, Henderson GS & Massiot D (2014). The role of al3 + on rheology and structural changes in sodium silicate and aluminosilicate glasses and melts. *Geochim Cosmochim Acta* **126**, 495–517. https://doi.org/10.1016/j.gca.2013.11.010

Leng Y (2013). *Materials Characterization: Introduction to Microscopic and Spectroscopic Methods*, 2nd ed. Weinheim: Wiley-VCH Verlag GmbH & Co. KGaA.

Lu X, Schreiber DK, Neeway JJ, Ryan JV & Du J (2017). Effects of optical dopants and laser wavelength on atom probe tomography analyses of borosilicate glasses. *J Am Ceram Soc* **100**, 4801–4815. https://doi.org/10.1111/jace.14987

Malfait WJ, Zakaznova-Herzog VP & Halter WE (2008). Amorphous materials: Properties, structure, and durability: Quantitative Raman spectroscopy: Speciation of Na-silicate glasses and melts. *Am Minera* **93**, 1505–1518. https://doi.org/10.2138/am.2008.2783

Mysen BO (1990). Role of Al in depolymerized, peralkaline aluminosilicate melts in the systems $Li_2O$-$Al_2O_3$-$SiO_2$, $Na_2O$-$Al_2O_3$-$SiO_2$, and K2 O-$Al_2O_3$-$SiO_2$. *Am Mineral* **75**, 120–134.

Mysen BO (1998). Phosphorus solubility mechanisms in haplogranitic aluminosilicate glass and melt: Effect of temperature and aluminum content. *Contrib Mineral Petrol* **133**, 38–50. https://doi.org/10.1007/s004100050435

Nordberg ME, Mochel EL, Garfinkel HM & Olcott JS (1964). Strengthening by Ion exchange. *J Am Ceram Soc* **47**, 215–219. https://doi.org/10.1111/j.1151-2916.1964.tb14399.x

Oven R (2021*a*). Analytical model of electric field assisted ion diffusion into glass containing two indigenous mobile species, with application to poling. *J Non-Crystal Solids* **553**, 120476. https://doi.org/10.1016/j.jnoncrysol.2020.120476

Oven R. (2021*b*). Calculation of the space charge distribution in poled soda-lime glass. *J Phys Condens Matter* **34**, 55702. https://doi.org/10.1088/1361-648X/ac3305

SamsungDisplay (2020). Samsung Display Introduces Foldable Display with Easily Bendable, Ultra-thin Glass. *Samsung Newsroom U.S.*

Saxey DW (2011). Correlated ion analysis and the interpretation of atom probe mass spectra. *Ultramicroscopy* **111**, 473–479. https://doi.org/10.1016/j.ultramic.2010.11.021

Schenk ER & Almirall JR (2012). Elemental analysis of glass by laser ablation inductively coupled plasma optical emission spectrometry (LA-ICP-OES). *Forensic Sci Int* **217**, 222–228. https://doi.org/10.1016/j.forsciint.2011.11.009

Schnatter KH, Doremus RH & Lanford WA (1988). Hydrogen analysis of soda-lime silicate glass. *J Non-Crystal Solids* **102**, 11–18. https://doi.org/10.1016/0022-3093(88)90106-8

SCHOTT (2021). SCHOTT FLEXINITY® - Structured Glass Solutions.

Sglavo VM (2015). Chemical strengthening of Soda lime silicate float glass: Effect of small differences in the KNO3 bath. *Int J Appl Glass Sci* **6**, 72–82. https://doi.org/10.1111/ijag.12101

Sglavo VM, Talimian A & Ocsko N (2017). Influence of salt bath calcium contamination on soda lime silicate glass chemical strengthening. *J Non-Crystal Solids* **458**, 121–128. https://doi.org/10.1016/j.jnoncrysol.2016.12.023

Shan Z, Liu J, Liu M, Shi F, Wu C, Wang C & Liu T (2018). Surface strengthening of lithium disilicate glass-ceramic by ion-exchange using Rb, Cs nitrates. *Ceram Int* **44**, 12466–12471. https://doi.org/10.1016/j.ceramint.2018.04.037

Shariq A, Al-Kassab T & Kirchheim R (2012). Studying nearest neighbor correlations by atom probe tomography (APT) in metallic glasses as exemplified for Fe(40)Ni(40)B(20) glassy ribbons. *J Alloys Compound* **512**, 270–277. https://doi.org/10.1016/j.jallcom.2011.09.079

Stephenson LT, Moody MP, Liddicoat PV & Ringer SP (2007). New techniques for the analysis of fine-scaled clustering phenomena within atom probe tomography (APT) data. *Microsc Microanal* **13**, 448–463. https://doi.org/10.1017/S1431927607070900

Tanaka Y (2013). Electric actuating valves incorporated into an all glass-based microchip exploiting the flexibility of ultra thin glass. *RSC Adv* **3**, 10213–10220. https://doi.org/10.1039/c3ra41218k

Terakado N, Sasaki R, Takahashi Y, Fujiwara T, Orihara S & Orihara Y (2020). A novel method for stress evaluation in chemically strengthened glass based on micro-Raman spectroscopy. *Commun Phys* **3**, 37. https://doi.org/10.1038/s42005-020-0305-7

Thompson K, Lawrence D, Larson DJ, Olson JD, Kelly TF & Gorman B (2007). In situ site-specific specimen preparation for atom probe tomography. *Ultramicroscopy* **107**, 131–139. https://doi.org/10.1016/j.ultramic.2006.06.008

Tošić MB, Nikolić JD, Grujić SR, Živanović VD, Zildžović SN, Matijašević SD & Ždrale SV (2013). Dissolution behavior of a polyphosphate glass into an aqueous solution under static leaching conditions. *J Non-Crystal Solids* **362**, 185–194. https://doi.org/10.1016/j.jnoncrysol.2012.11.024

Varshneya AK (2010). Chemical strengthening of glass: Lessons learned and yet to be learned. *Int J Appl Glass Sci* **1**, 131–142. https://doi.org/10.1111/j.2041-1294.2010.00010.x

Wang HF, Xing GZ, Wang XY, Zhang LL, Zhang L & Li S (2014). Chemically strengthened protection glasses for the applications of space solar cells. *AIP Adv* **4**, 47133. https://doi.org/10.1063/1.4873538

Wang Z, Liu J, Zhou Y, Neeway JJ, Schreiber DK, Crum JV, Ryan JV, Wang X-L, Wang F & Zhu Z (2016). Nanoscale imaging of Li and B in nuclear waste glass, a comparison of ToF-SIMS, NanoSIMS, and APT. *Surf Interface Anal* **48**, 1392–1401. https://doi.org/10.1002/sia.6049

Williams, G. A. & Ferguson, J. B. (1922). THE DIFFUSION OF HYDROGEN AND HELIUM THROUGH SILICA GLASS AND OTHER GLASSES1. *J Am Chem Soc* **44**, 2160–2167. https://doi.org/10.1021/ja01431a010

Xiang Y, Du J, Smedskjaer MM & Mauro JC (2013). Structure and properties of sodium aluminosilicate glasses from molecular dynamics simulations. *J Chem Phys* **139**, 44507. https://doi.org/10.1063/1.4816378

Xiangchen Z, Ouli H, Cengzuo X & Yinghuan Z (1986). The effect of impurity ions in molten salt KNO3 on ion-exchange and strengthening of glass. *J Non-Crystal Solids* **80**, 313–318. https://doi.org/10.1016/0022-3093(86)90412-6

Yalikun Y & Tanaka Y (2017). Ultra-thin glass sheet integrated transparent diaphragm pressure transducer. *Sens Actuators A Phys* **263**, 102–112. https://doi.org/10.1016/j.sna.2017.05.047

Yan Y, Faber AJ & de Waal H (1996). Structural role of aluminum ions in sodium aluminophosphate glasses. *J Am Ceram Soc* **79**, 286–288. https://doi.org/10.1111/j.1151-2916.1996.tb07912.x

Yao L, Cairney JM, Gault B, Zhu C & Ringer SP (2013). Correlating spatial, temporal and chemical information in atom probe data: New insights from multiple evaporation in microalloyed steels. *Philos Mag Lett* **93**, 299–306. https://doi.org/10.1080/09500839.2013.771823

Yao L, Gault B, Cairney JMMM & Ringer SPPP (2010). On the multiplicity of field evaporation events in atom probe: A new dimension to the analysis of mass spectra. *Philos Mag Lett* **90**, 121–129. https://doi.org/10.1080/09500830903472997

Yoo S-H, Kim S-H, Woods E, Gault B, Todorova M & Neugebauer J (2022). Origins of the hydrogen signal in atom probe tomography: Case studies of alkali and noble metals. *New J Phys* **24**, 13008. https://doi.org/10.1088/1367-2630/ac40cd

Yuan Y, Yalikun Y, Amaya S, Aishan Y, Shen Y & Tanaka Y (2021). Fabrication of ultra-thin glass sheet by weight-controlled load-assisted precise thermal stretching. *Sens Actuators A Phys.* **321**, 112604. https://doi.org/10.1016/j.sna.2021.112604

Zanuttini D, Blum I, Rigutti L, Vurpillot F, Douady J, Jacquet E, Anglade P-M & Gervais B (2017). Simulation of field-induced molecular dissociation in atom-probe tomography: Identification of a neutral emission channel. *Phys Rev A* **95**, 61401. https://doi.org/10.1103/PhysRevA.95.061401

Zeng H, Wang L, Ye F, Yang B, Chen J, Chen G & Sun L (2016). Mechanical–structural investigation of chemical strengthening aluminosilicate glass through introducing phosphorus pentoxide. *Front Materials* **3**, 53. https://doi.org/10.3389/fmats.2016.00053